Real-Time Estimation and Damping of SSR in a VSC-HVDC Connected Series-Compensated System

Tibin Joseph , *Member, IEEE*, Carlos E. Ugalde-Loo , *Member, IEEE*, Senthooran Balasubramaniam, *Student Member, IEEE*, and Jun Liang , *Senior Member, IEEE*

Abstract—**Infrastructure reinforcement using high-voltage direct-current (HVDC) links and series compensation has been proposed to boost the power transmission capacity of existing ac grids. However, deployment of series capacitors may lead to subsynchronous resonance (SSR). Besides providing bulk power transfer, voltage source converter (VSC)-based HVDC links can be effectively used to damp SSR. To this end, this paper presents a method for the real-time estimation of the subsynchronous frequency component present in series-compensated transmission lines—key information required for the optimal design of damping controllers. A state-space representation has been formulated and an eigenvalue analysis has been performed to evaluate the impact of a VSC-HVDC link on the torsional modes of nearby connected thermal generation plants. Furthermore, the series-compensated system has been implemented in a real-time digital simulator and connected to a VSC-HVDC scaled-down test-rig to perform hardware-in-the-loop tests. The efficacy and operational performance of the ac/dc network while providing SSR damping is tested through a series of experiments. The proposed estimation and damping method shows a good performance both in time-domain simulations and laboratory experiments.**

Index Terms—**Subsynchronous resonance (SSR), high-voltage direct-current (HVDC), eigenanalysis, series compensation, real-time estimation, voltage source converter (VSC).**

I. INTRODUCTION

SERIES compensation is a well-known method to enhance thermal and stability limits of long transmission lines. However, its use brings the potential risk of subsynchronous resonance (SSR), where the electrical modes of compensated lines interact with the mechanical modes of nearby thermal generation

plants [1]. This interaction may result in torsional oscillations on the shafts of generators which, if left unattended, may lead to fatigue and ultimately failure [1]–[3].

Transmission network reinforcement using HVDC links is now a well-established alternative to series compensation. This technology has proven to be reliable, providing advanced functionality to network operators [4], [5]. Compared to line commutated converter (LCC) based HVDC, the voltage source converter (VSC) based technology is gaining momentum due to its inherent advantages [6]. VSC-HVDC links are being connected in parallel with existing LCC links to further enhance the power transfer capability of already compensated ac systems [4], [5]. Although it has been shown that LCC-HVDC systems connected to turbo-generating units may destabilize torsional modes and lead to torsional interactions [7], this is not the case for most operating conditions of VSC-HVDC systems [8]. However, destabilization of torsional dynamics using VSC-HVDC has been also reported [9], [10] and, thus, its impact on torsional modes has to be carefully evaluated before exploring its capability for SSR damping. SSR has been lately reported in wind turbines and series-compensated transmission lines; thus, SSR monitoring and damping are still of great practical significance [11], [12]. Recent research has recognized this, with a number of monitoring and detection schemes [13], [14], [17] and techniques to damp SSR [18]–[24] being proposed.

Phasor measurement units (PMUs) have been proposed for the online monitoring and detection of subsynchronous torsional oscillations [13], [14]. The generator speed is used as an input signal for the damping schemes, which requires communication with the compensating devices. This may affect the reliability of the damping controller as system stability could be compromised under communication delays. Research efforts have been made to account for time delays in transient stability studies. For instance, nonlinear control strategies for communication time delay compensation using PMUs have been proposed to enhance transient stability margins [15], [16]. However, existing PMUs cannot efficiently monitor the wide range of SSR frequencies [5]. To avoid the use of communications, local measurements may be employed to estimate subsynchronous frequency (SSF) components [17], [19], [22]. Potential alternatives include the use of low-pass filter and recursive least square based estimation and damping methods [19], [21]; Kalman filters [17]; and multi-modal damping [22]. It can be concluded from these

studies that the use of local measurements for detecting and damping SSF components could be a reliable, cost-effective and robust alternative compared to communication-based methods.

Most PMU or local measurement-based estimation schemes use FACTS devices or HVDC stations for damping purposes [18]–[21]. The use of a static series synchronous compensator (SSSC) and a static synchronous compensator (STATCOM) for SSR damping has been reported in [17], [18], [21]. Recently, VSCs have been used explicitly for providing SSR damping in series-compensated transmission lines [24], [25]. In all these cases the devices were used solely for the purpose of damping without much discussion on their basic functionality and operation under an SSR event. Studies on passive SSR damping schemes and experimental tests have been reported in [25], [26], [29]. In passive schemes, damping is achieved by reshaping the output admittance of the VSC. However, compared with active schemes, passive mitigation methods cannot track and compensate multiple SSF components automatically; thus, they exhibit an inferior SSR suppression performance.

Another aspect which demands attention is the lack of availability of turbo-generator shaft data, which limits the adaptability of damping schemes to multiple modes of oscillations. Real-time estimation and tracking of subsynchronous electrical modes at any series compensation level can help to overcome this issue, preventing interactions with the mechanical shaft modes—irrespective of their values. To contribute to this effort, this paper proposes an adaptive subsynchronous frequency damping controller (SSFDC) capable of estimating and damping SSF components regardless of the configuration of the power system. For completeness, the adaptive damping scheme is tested on a real-time experimental test-rig.

Although [29] constitutes a good attempt to experimentally damp SSR, its practical contribution is limited as the exact knowledge of SSF components is a pre-requisite for a successful performance. The work presented in this paper goes beyond that initial effort by providing an adaptive structure that is capable of identifying, in real-time, SSF components and damping them regardless of their values. In other words, the scheme proposed in this work would be useful even when generator data is not available. In addition, the stability assessment of the whole system, including the GB system, the HVDC link and all controllers, is provided for completeness.

The main contributions of the paper are: (1) quantification of SSR in a series-compensated ac/dc network using a detailed state-space system model and eigenanalysis; (2) design of an adaptive SSFDC which can identify, track and damp multiple SSF modes; (3) unlike previous research work studying SSR using theoretical analysis and time-domain simulations, the present work utilizes a real-time hardware-in-the-loop (RT-HiL) experimental platform for the validation of the SSFDC-equipped VSC-HVDC link. Detailed SSR eigenanalysis is carried out in an ac/dc system resembling the reduced Great Britain (GB) power system. The effectiveness of the proposed SSFDC scheme to damp multiple torsional modes while providing basic functionality of power transfer has been validated through time-domain simulations and RT-HiL experiments.
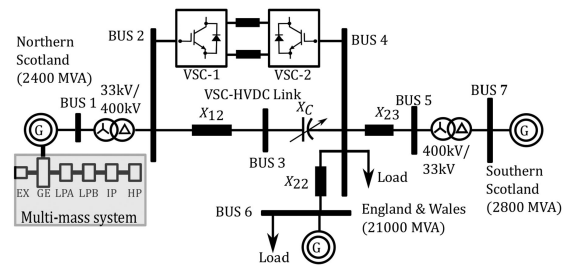

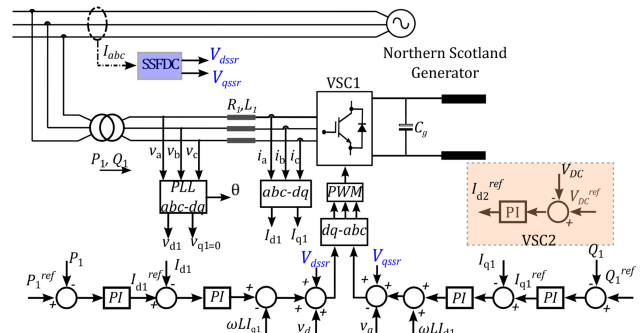Fig. 1. GB three-machine system configuration with reinforcements.

Fig. 2. Rectifier VSC with main and auxiliary control loops (VSC1).

II. SYSTEM CONFIGURATION AND MODELING

IEEE First and Second Benchmark Models (FBM and SBM) have been traditionally used to obtain a good understanding of SSR [27], [28]. As such, they are suitable for designing SSFDCs [23], [26]. These models have been extended to the network shown in Fig. 1 to assess the impact of VSC-HVDC links in a simplified GB mainland system splitting into three major generation areas: England and Wales (E&W), Southern Scotland (SS) and Northern Scotland (NS), with respective ratings of 21000, 2800 and 2400 MVA [30]. The NS generator model includes a multi-mass shaft with six turbine masses as in the FBM. The remaining machines were modeled as single-mass turbo-generators. The test system has been previously used for SSR studies in a reinforced GB system [29]–[32].

Infrastructure upgrades are in line with those proposed by National Grid (UK's transmission system operator and owner)—aiming to facilitate the export of additional wind power from Scotland to major load centres in the South without the construction of new overhead lines. Reinforcements consist of series compensation in the inland network and submarine HVDC links between E&W and SS [4], [5]. Although it could be argued that the adopted network is a rather simple version of the GB system, it provides enough information to study, understand and test SSR in a multi-machine ac/dc system.

A. VSC-HVDC Link Control

The primary design objectives of a VSC-HVDC link are active power transfer and reactive power support to the grid. The variables to be controlled are the active and reactive power (at both terminals) and dc voltage. Fig. 2 illustrates the main control strategy for the rectifier station (VSC1) and the dc voltage control at the inverter station (VSC2). A dq reference frame is
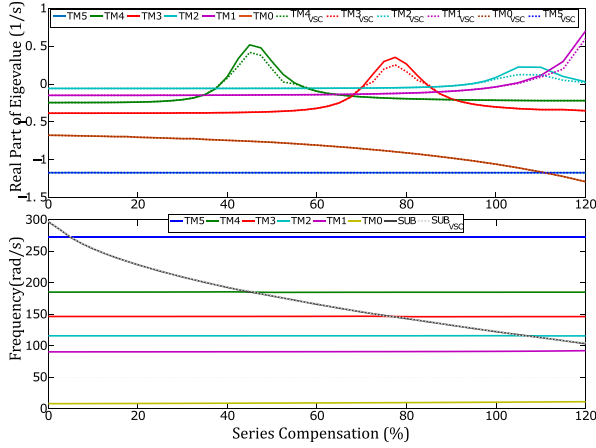
Fig. 3. Stability of the torsional modes in terms of series compensation. Dashed lines are used for an HVDC-upgraded system.

adopted and a cascaded control structure based on PI controllers is used [8], [32]. For modeling details of the VSC-HVDC link the reader is referred to [32], [33]. The control parameters are included in the Appendix for completeness.

B. State-Space Modeling

A detailed state-space model of the system shown in Fig. 1 has been developed. It includes the dynamic equations of the synchronous machines, transmission lines and the HVDC link with its controllers as given by (1)–(4). This is a system of 77 differential equations linearized around an operating point. The state equation and state vector are, respectively, given by

$$\Delta \dot{X}_{sys} = A_{sys} \Delta X_{sys} \tag{1}$$

$$\Delta X_{sys} = [X_{NG}, X_{N\omega}, X_{N\theta}, X_{SG}, X_{EWG}, X_T, X_{DC}]^T \tag{2}$$

where X_{NG}, $X_{N\omega}$, $X_{N\theta}$, constitute the states associated with the NS generator; X_T, the series-compensated transmission line; X_{SG}, X_{EWG}, the SS and E&W generators; and X_{DC}, the VSC-HVDC link. The transmission line connecting the NS generator has been upgraded with series compensation. The VSC-HVDC link is connected between Buses 2 and 4.

System (1) has been constructed in MATLAB to perform eigenanalysis. It is characterized by four unstable torsional modes (TM1–TM4) associated with the NS generator shaft which may be excited at different compensation levels. Fig. 3 shows the ranges of compensation for which torsional instability arises. Stability is directly related to the subsynchronous mode (SUB) of the HVDC-connected series-compensated transmission line linked to the NS generator. Instability occurs when SUB is in the neighborhood of a TM frequency, as shown by the real part of the eigenvalues of TM1–TM4. For further information on system modeling, the reader is referred to [30]–[32], where complete linearized models of the synchronous generator with a multi-mass shaft and a VSC-HVDC link with its controllers are provided. Due to space limitations, the full state-space model is not included in the paper.

Table I summarizes the relevant eigenvalues for 30, 40 and 75% series compensation. As it can be seen, when 30% of com-

TABLE I
RELEVANT EIGENVALUES

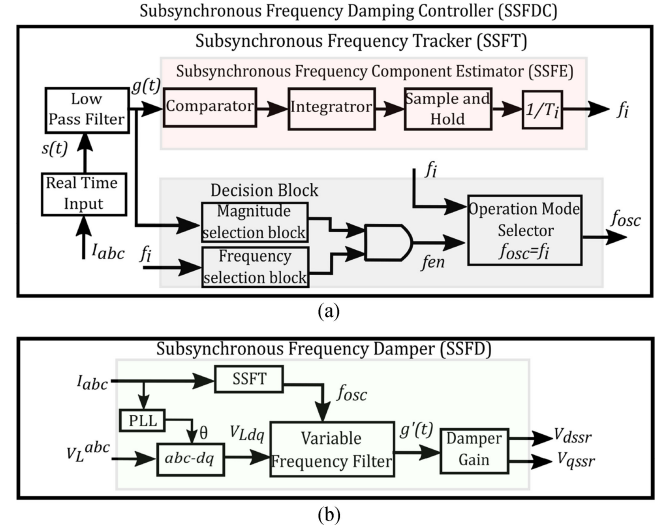| TM	30% Compensation	40% Compensation	75% Compensation
TM5	$-1.173 \pm j272.193$	$-1.173 \pm j272.183$	$-1.173 \pm j272.193$
TM4	$-0.207 \pm j185.488$	$+0.097 \pm j187.925$	$-0.185 \pm j185.099$
TM3	$-0.383 \pm j146.666$	$-0.379 \pm j146.56$	$+0.297 \pm j146.825$
TM2	$-0.058 \pm j115.970$	$-0.058 \pm j114.75$	$-0.051 \pm j116.012$
TM1	$-0.149 \pm j90.574$	$-0.147 \pm j91.123$	$-0.128 \pm j90.868$
SUB	$-7.443 \pm j209.289$	$-7.674 \pm j191.574$	$-7.735 \pm j148.310$
SUPER	$-8.518 \pm j418.520$	$-8.665 \pm j432.55$	$-9.110 \pm j479.435$

Fig. 4. Block diagram of the proposed SSFDC: (a) SSFT. (b) SSFD.

pensation is employed the system is stable. However, for 40% SUB ($\simeq$30.7 Hz) interacts with TM4 of the shaft ($\simeq$29.6 Hz). As a consequence, SSR arises and TM4 becomes unstable, evidenced by its positive real part. Similarly, for 75% SUB ($\simeq$23.61 Hz) interacts with TM3 of the shaft ($\simeq$23.37 Hz), resulting in unstable oscillations in the system evidenced by the positive real part of TM3. For these operating conditions any small disturbance or load change would trigger SSR.

III. DAMPING CONTROLLER

To damp SSR upon occurrence, a supplementary SSFDC has been designed and integrated with the control loop of VSC1. Its main objective is to increase the network damping at critical frequencies of the turbo-generator shaft. This is achieved by suppressing the line current component at SSFs (see Fig. 2). Fig. 4 shows a block diagram representation of the SSFDC. It is formed by an SSF tracker (SSFT), which estimates and tracks the frequency component in the line current upon an SSR event, and by an SSF damper (SSFD), which utilizes the tracked frequency component to generate a $180°$ anti-phase signal to be injected at the point of common coupling (PCC) with the VSC station. In general a voltage signal with a SSF component can be represented as:

$$s(t) = A_1 \sin(2\pi f t + \theta_1) + \sum_{k=2}^{m} A_k \sin(2\pi f_k t + \theta_k)$$

$$= A_1 \sin(2\pi f t + \theta_1) + \sum_{k=2}^{m} [A_k \sin(2\pi f_k t) \cos(\theta_k)$$

$$+ A_k \cos\left(2\pi f_k t\right)\sin\left(\theta_k\right)]$$

$$= A_1 \sin\left(2\pi f t + \theta_1\right) + \sum_{k=2}^{m}[A_k \sin\left(2\pi f_k t\right)$$

$$+ A_k \cos\left(2\pi f_k t\right)]$$

$$= x(t) + g(t), \tag{3}$$

where f is the fundamental frequency; A_k, θ_k, the amplitude and phase angle of the k-th component, which includes SUB and super-synchronous (SUPER) components; and m the total number of torsional modes. In (3), $x(t)$ is the fundamental frequency signal and $g(t)$ encapsulates the SSF component of $s(t)$. As explained in [21], the network exhibits a small positive damping for frequencies above the fundamental. Therefore, the SUPER component is not of interest. The SSFDC aims to cancel $g(t)$ from $s(t)$ to obtain $x(t)$. In the proposed method, the frequency component of $g(t)$ is first detected and tracked upon occurrence of SSR. Then a compensation signal $g'(t)$ is generated to cancel out $g(t)$.

A. Subsynchronous Frequency Tracker

During an SSR event, the frequency of the line current will deviate from its nominal value and will begin to oscillate. When the frequency of oscillation (f_{osc}) coincides with the complement of the frequency of a generator shaft torsional mode (f_{tm}), the oscillations will be sustained [2], [3]. An SSFT can be designed to identify and track f_{osc}.

As seen from Fig. 4(a), the SSFT is comprised mainly of an SSF component estimator (SSFE) and a decision block. The ac line current is fed to the SSFE through a low-pass filter, which isolates $g(t)$ and eliminates the driving frequency component $x(t)$ at 50 Hz. This is the input signal to the SSFT block, which through a series of transformations identifies the SSF component (f_i) in the line current. Once this network mode is identified, a decision block is used to track the magnitude of $g(t)$. This is compared with f_i to avoid a tracking operation when no oscillation is observed. An operating mode selector is utilized to enable the output of SSFT, which is the tracked oscillation frequency f_{osc}. It should be emphasized that the tracking of f_{osc} could be done regardless of the configuration of the power system since the natural frequencies of a turbo-generator shaft can be considered as constant [2].

B. Subsynchronous Frequency Damper

The second stage in the SSFDC design process is to generate signal $g'(t)$ to eliminate the SSF component (f_{osc}). To serve this purpose, the SSFD shown in Fig. 4(b) has been designed and implemented. It is formed by a variable frequency filter and a damper gain. The output of the SSFT is used as the central frequency of the filter, whose input is the dq voltage at the PCC—obtained using a suitable reference frame transformation block and synchronized using a phase-locked loop (PLL). The filter outputs the target signal fed to the damper gain block to produce a $180°$ phase shift to create $g'(t)$. Following a coordinate transformation, damping components v_{dssr} and v_{qssr} are generated. These are added to the primary control voltage

TABLE II
EIGENVALUES OF THE COMBINED SYSTEM WITH SSFDC

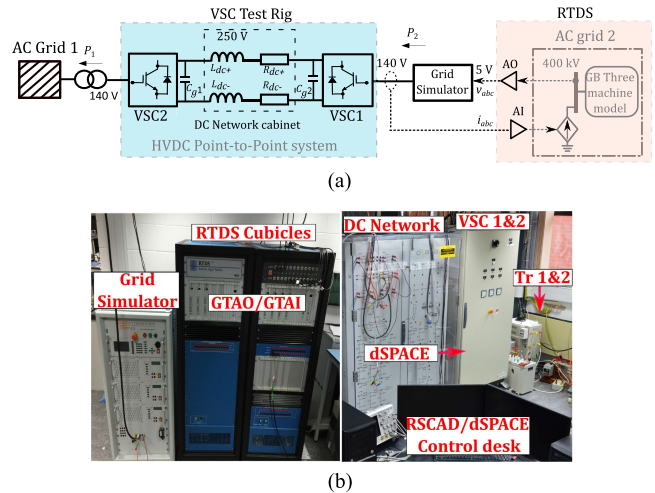| TM	40% Compensation	75% Compensation
TM5	$-1.173 \pm j272.183$	$-1.173 \pm j272.192$
TM4	$-0.857 \pm j184.613$	$-0.182 \pm j184.112$
TM3	$-0.379 \pm j144.561$	$-0.576 \pm j144.314$
TM2	$-0.056 \pm j117.89$	$-0.054 \pm j115.210$
TM1	$-0.149 \pm j90.521$	$-0.121 \pm j89.931$
SUB	$-2.871 \pm j234.930$	$-1.543 \pm j229.421$
SUPER	$-6.325 \pm j436.238$	$-7.012 \pm j480.198$

(a)

(b)

Fig. 5. RT-HiL configuration. (a) Connection diagram. (b) Physical rig set-up.

reference signals v_d and v_q of VSC1 (see Fig. 2). The resultant voltage at the converter terminals will damp SSR in the ac network by effectively eliminating $g(t)$ in $s(t)$.

Table I summarizes the relevant eigenvalues for 30, 40 and 75% series compensation. As it can be seen, when 30% of compensation is employed the system is stable. However, for 40% SUB ($\simeq 30.7$ Hz) interacts with TM4 of the shaft ($\simeq 29.6$ Hz). As a consequence, SSR arises and TM4 becomes unstable, evidenced by its positive real part. Similarly, for 75% SUB ($\simeq 23.61$ Hz) interacts with TM3 of the shaft ($\simeq 23.37$ Hz), resulting in unstable oscillations in the system evidenced by the positive real part of TM3. For these operating conditions any small disturbance or load change would trigger SSR.

The relevant eigenvalues of the SSFDC-upgraded system are summarized in Table II. As it can be observed, once the damper is in operation, the frequency of SUB shifts away from that of TM3 and TM4. As a result, the system is stable, with TM3 and TM4 now exhibiting a negative real part.

IV. RT-HiL EXPERIMENTAL SET-UP

It is difficult to investigate and test SSR damping schemes in practical power systems. However, a good approximation can be achieved using the RT-HiL experimental platform shown in Fig. 5. It consists of a real-time digital simulator (RTDS), a grid simulator (GS), and an HVDC test-rig. To perform RT-HiL tests, the system shown in Fig. 1 was modeled in the RSCAD software of the RTDS. High voltages were converted to a low voltage using the GS, which were in turn interfaced with the HVDC test-rig through the analogue output (AO) cards of the

TABLE III
TEST-RIG SPECIFICATIONS AND PARAMETERS

Devices	Specifications	Rating
Converters	Rated power Rated ac voltage Rated dc voltage Topology	1 kW (1 p.u.) 140 V 250 V (1 p.u.) Two-level, symmetrical monopole
AC inductors	L_{g1}, L_{g2}	2.2 mH
DC lines	L_{dc}, R_{dc}	2.4 mH, 0.26 Ω
DC capacitors	C_{g1}, C_{g2}	1020 μF
Control system	dSPACE DS1005/ControlDesk 3.2 (Simulink interface)	
Real-time simulator	RTDS/RSCAD, Racks: 2. Cards: 2 GTWIF, 4 PB5 (2 GTDI, 2 GTDO, 2 GTAI, 2 GTAO, 2 GTNET)	

RTDS firmware. The GS produces a three-phase mains supply voltage from the GTAO cards of the RTDS. This is achieved by using a four-quadrant amplifier rated at 2 kVA and 270 V (line-to-ground rms). To close the loop between the RTDS and the HVDC rig, the three-phase line current is tapped and fed to the analogue input (AI) card of the RTDS (see Fig. 5(a)).

The HVDC test-rig is formed by two VSCs, two transformers, a dc line cabinet and a dSPACE DS1005 controller. The VSCs are operated at a rated power of 1 kW, 140 V ac and $\pm$125 V dc. A conversion ratio of 400 kV/140 V is achieved using the GS. The output voltage of the GS is controlled using an autotransformer. The dSPACE platform acquires data and monitors system states of the test-rig and controls each VSC. The hardware set-up is shown in Fig. 5(b). The RTDS and VSC-HVDC test-rig parameters are summarized in Table III.

V. RT-HiL EXPERIMENTAL RESULTS

Experiments were carried out on the RT-HiL platform to validate the effectiveness of the SSFDC to provide damping at selected SSFs and to assess its impact on the converter performance. For comparison purposes, the performance of the integrated ac/dc system shown in Fig. 1 was evaluated with and without the use of an SSFDC. To assess system stability, two scenarios have been considered:

- Case A: Change in compensation level from 30 to 40%.
- Case B: Change in compensation level from 30 to 75%.

In both cases, the change in series compensation occurs at $t = 4$ s into the simulation. This is achieved by suitably modifying the value of X_c.

A. Integrated AC/DC System Without SSFDC

Figs. 6 to 8 show the RT-HiL experimental results for Cases A and B without the use of an SSFDC. The occurrence of SSR is evidenced in Figs. 6(a) and 6(b) by the rise in the magnitude of line current from its rated value. The dominant SSF components for the new compensation values ($\simeq$ 20 Hz for 40% compensation and $\simeq$ 27 Hz for 75% compensation) are evidenced in Figs. 6(c) and 6(d)—obtained using a fast Fourier transform (FFT) spectrum analysis. The information provided by Fig. 6 agrees on well with the eigenanalysis presented in Section III-C: at 40% compensation TM4 ($\simeq$ 30 Hz) is excited as this is the
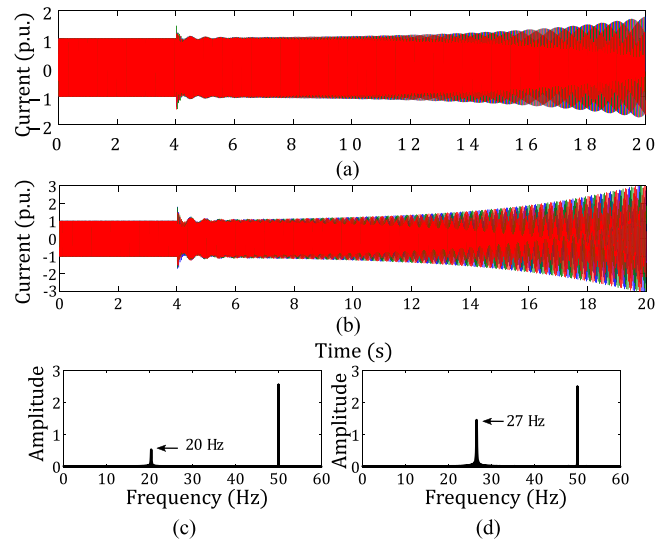

Fig. 6. Experimental results (RTDS signals) without SSFDC. Line currents. (a) Case A. (b) Case B. Spectrum of phase a output current. (c) Case A. (d) Case B.
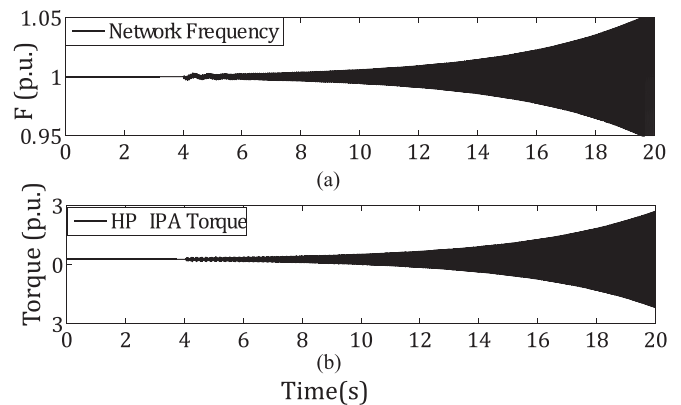

Fig. 7. Experimental results (RTDS signals) without SSFDC for Case A. (a) Frequency of phase a current of the NS generator. (b) Selected torque interactions in the multimass shaft of the NS generator.

complement of the network SUB mode ($\simeq$ 20 Hz); conversely, at 75% compensation TM3 ($\simeq$ 23 Hz) is excited as this is the complement of the corresponding SUB mode ($\simeq$ 27 Hz). It is clear from the plots that without proper control methods the network SSF component increases in magnitude and the system becomes unstable.

Fig. 7 shows the frequency and torque responses for Case A only. Since the plots for Case B exhibit a similar behavior no further discussion is warranted. Fig. 7(a) shows the network frequency, which starts deviating from 1 p.u. (50 Hz) due to SSR following the change in series compensation. Fig. 7(b) depicts the selected torque response in the shaft of the NS generator. As it can be observed, the system is unstable as predicted by the eigenanalysis (see Fig. 3 and Table I).

Fig. 8 shows the dq voltages (V_d, V_q) at the PCC, the dc link voltage (V_{dc}), and the output power (P_1) of VSC1 at Bus 2. The results reveal that the magnitude of these variables increases following the change in compensation. If no
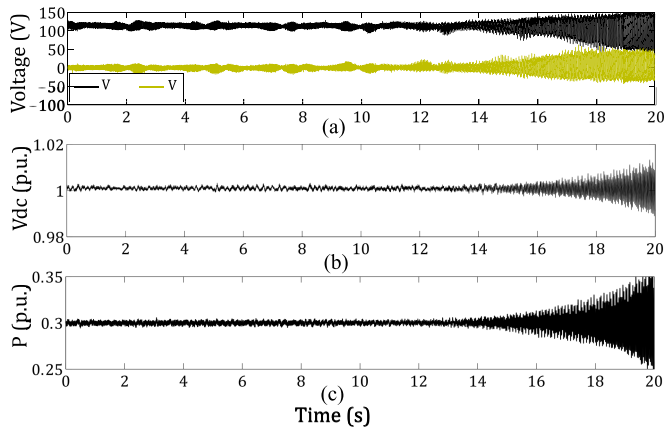
Fig. 8. Experimental results (HVDC test-rig signals) without SSFDC for Case A. (a) dq voltage. (b) DC-link voltage. (c) Output power at VSC1.
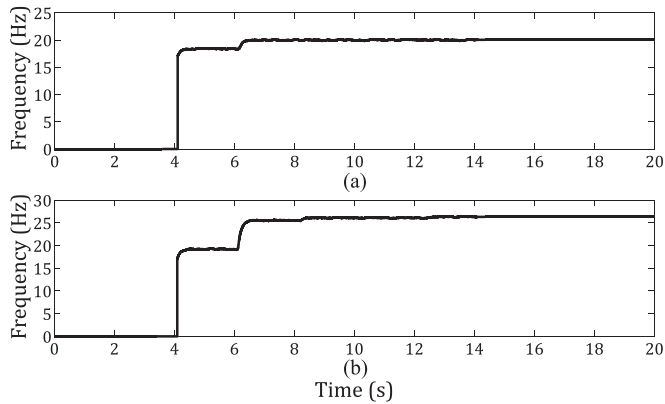

Fig. 9. Network oscillation frequency (f_{osc}) tracking performance at around. (a) 20 Hz (Case A). (b) 27 Hz (Case B).
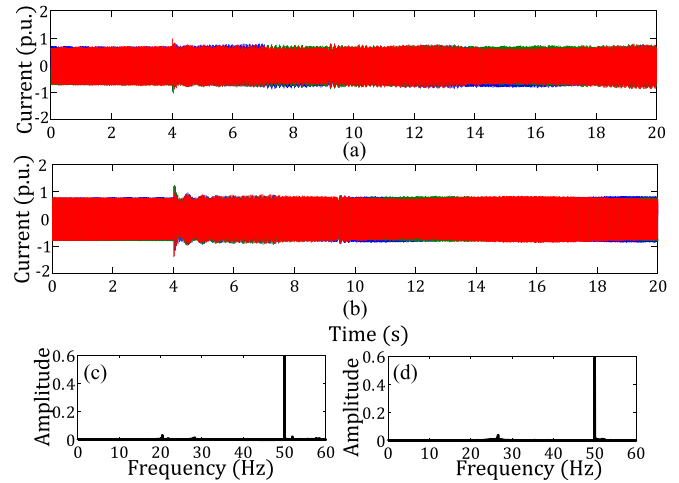

Fig. 10. Experimental results (RTDS signals) with SSFDC in operation. Line currents. (a) Case A. (b) Case B. Spectrum of phase a output current. (c) Case A. (d) Case B.

Fig. 11. Experimental results (RTDS signals) with SSFDC in operation for Case A. (a) Frequency of phase a current of the NS generator. (b) Selected torque interactions in the multimass shaft of the NS generator.

corrective measures are taken these oscillations will surpass the converter limits. Fig. 8(a) shows the converter dq ac voltage. It can be observed that the SSF component is transferred into the ac side voltage. Converter instability is evidenced by the dc voltage and power output (see Figs. 8(b) and 8(c)). In all cases the oscillations build up over a long period ($\simeq 16$ s), which is a natural result of low frequency instability associated with SSFs [26]. It can concluded that the VSC on its own does not provide sufficient system damping following a change in series compensation. Without proper countermeasures, the operation of the ac/dc network could be compromised due to SSR.

B. Integrated AC/DC System With SSFDC

The control loop of VSC1 is upgraded with an SSFDC, with experimental results shown in Figs. 9 to 14. Using the SSFE and SSFT described in Section IV, the network SSF component (f_{osc}) for Cases A and B is successfully identified, as shown in Fig. 9. For Case A, the SSFT is able to track the dominant SSF component ($\simeq 20$ Hz) in less than $\simeq 2.5$ s (see Fig. 9(a)). A similar response is observed for Case B, where the dominant mode ($\simeq 27$ Hz) is also tracked (see Fig. 9(b)). These results

agree on well with the FFT spectra in Figs. 6(c)–(d) and with the eigenvalues from Table I.

The line current plots and their frequency spectra are shown in Fig. 10. The change in series compensation produces initial increasing oscillations in both cases. However, once the SSFT identifies and tracks the exact network mode, the SSFDC acts at $t \simeq 7$ s into the simulation by injecting the anti-phase signal and, consequently, is able to damp SSR (see Figs. 10(a) and 10(b)). The network SSF components interacting with the mechanical modes are identified, tracked and damped in less than 3.5 s and this is evidenced by Figs. 10(c) and 10(d).

Figs. 11 and 12 show the frequency of the phase a current and selected torque responses of the NS generator. An initial transient caused by the change in series compensation results in a frequency deviation from its nominal value and an increase in torque oscillations. Once the SSFDC operates, the shaft oscillations are damped out and steady-state operation is reached. These plots reveal the successful damping of multiple torsional modes—afforded by a correct SSF component tracking.
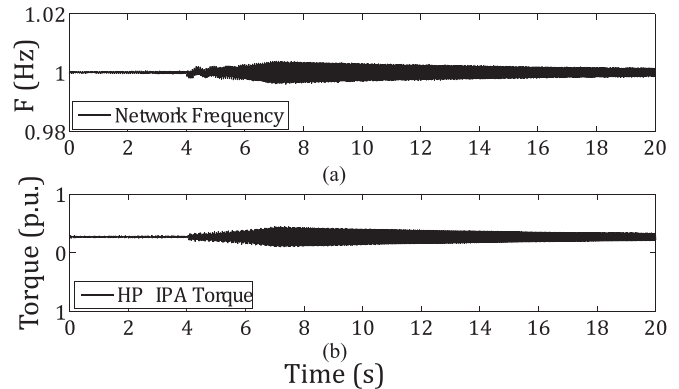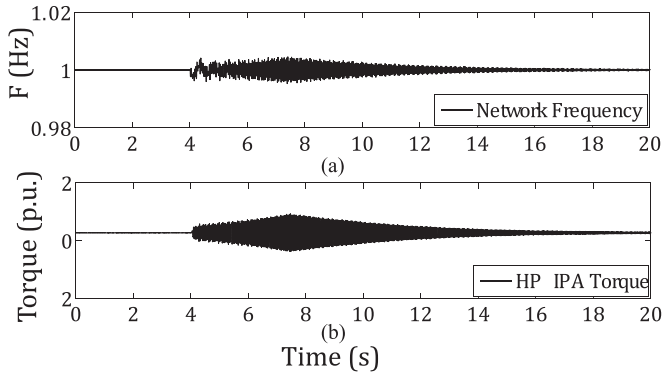
Fig. 12. Experimental results (RTDS signals) with SSFDC in operation for Case B. (a) Frequency of phase a current of the NS generator. (b) Selected torque interactions in the multimass shaft of the NS generator.
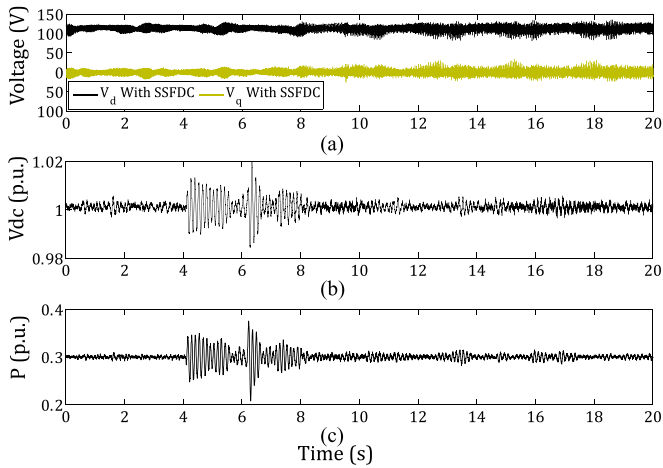

Fig. 13. Experimental results (HVDC rig signals) with SSFDC in operation for Case A. (a) dq voltage. (b) DC link voltage. (c) Output power at VSC1.

Fig. 14. Experimental results (HVDC rig signals) with SSFDC in operation for Case B. (a) dq voltage. (b) DC link voltage. (c) Output power at VSC1.

Fig. 15. Simulation results. (a) DC link output power at VSC1 with and without an SSFDC. (b) Selected torque interaction in the multimass shaft of the NS generator with and without an SSFDC.

Fig. 16. Experimental results. (a) DC link output power at VSC1 with and without an SSFDC. (b) Selected torque interaction in the multimass shaft of the NS generator with and without an SSFDC.

Figs. 13 and 14 show the responses of the VSC. The contribution of the SSFDC is evident and the stable performance of the converter is reflected in the ac voltage and its dq components (see Figs. 13(a) and 14(a)). The dc link voltage (V_{dc}) and the dc power (P) at VSC1 follow the dynamic pattern of the ac system response (see Figs. 13(b)–(c) and 14(b)–(c)). Initially, V_{dc} and P deviate from their nominal values, but once the SSFDC operates the oscillations disappear and steady-state is reached within seconds.

The results presented in this section show that the active damping compensation afforded by the proposed SSFDC stabilizes the system. A good performance is achieved for different modes of oscillation. Moreover, the additional support provided by VSC1 is within the converter capability and thus does not affect the normal operation of the HVDC link.

Although the main purpose of the paper is to provide evidence of a successful experimental performance of the proposed damping scheme, it should be emphasized that the RT-HiL results agree on well with those obtained via simulations. As shown in Figs. 15–16, a good performance is observed for Case A in both instances. This validates the effectiveness of the SSFDC-equipped VSC-HVDC link to provide SSR damping.
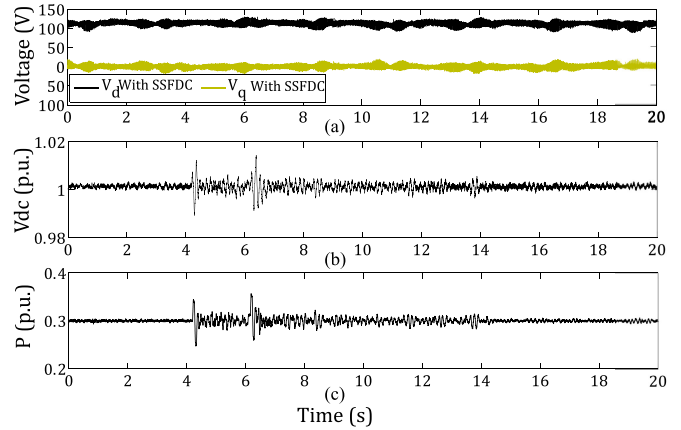
C. On the Use of the RT-HiL Platform

HiL enables the development and testing of complex embedded systems in real-time. In an RT-HiL platform, a mathematical representation related to complex system dynamics (in this case, the GB power system) interacts with the embedded system under study (the VSC-based HVDC link and its controllers). This way, the complexity of the plant under control is fully included in the test. RT-HiL can be used to model dangerous operating conditions—such as SSR occurrence.

TABLE IV
TORSIONAL STIFFNESS VARIATION

Shaft	K_{min}(p.u.)	K_{org}(p.u.)	K_{max} (p.u.)
HP-IP	15.44	19.303	23.16
IP-LPA	27.94	34.929	41.91
LPA-LPB	41.63	52.038	62.44
LPB-GEN	56.68	70.852	85.02
GEN-EX	2.25	2.822	3.38

TABLE V
EFFECT OF TORSIONAL STIFFNESS VARIATION IN EIGENVALUES

TM	K_{min}	K_{org}	K_{max}
TM5	$-1.173 \pm j243.44$	$-1.173 \pm j272.183$	$-1.173 \pm j298.170$
TM4	$-0.20 \pm j165.96$	$+0.097 \pm j187.925$	$+0.075 \pm j193.45$
TM3	$-0.383 \pm j131.21$	$-0.379 \pm j146.56$	$-0.371 \pm j160.69$
TM2	$-0.058 \pm j103.69$	$-0.058 \pm j114.75$	$-0.057 \pm j126.991$
TM1	$-0.151 \pm j81.14$	$-0.147 \pm j91.123$	$-0.144 \pm j99.185$
SUB	$-7.368 \pm j192.98$	$-7.674 \pm j192.75$	$-7.659 \pm j202.63$
SUPER	$-8.665 \pm j434.76$	$-8.665 \pm j432.55$	$-8.665 \pm j434.76$

By adopting the RT-HiL test-bench shown in Fig. 5, it is possible to assess the suitability of simulation-based models and to validate, in real-time, the feasibility of the damping strategy proposed in this work. Given the disruptive and dangerous nature of SSR and the potential damage that it may cause not only to power system plant, but also to personnel, the approach presented in this paper would enable a transmission system operator to reduce the risk of integrating SSR detection and damping schemes to a practical power system without subjecting it to permanent damage.

VI. DISCUSSION ON ROBUSTNESS AND UNCERTAINTY

A. Impact of Torsional Stiffness Uncertainty on SSF

Parametric variation in spring constants (torsional stiffness) can change the TMs of the turbine-masses and, as a result, shift the resonant frequencies in series-compensated transmission lines [34]. This may affect the tuning of SSFDCs. To account for torsional stiffness uncertainty and to assess its impact on SSF measurement and damping, variations of $\pm20\%$ to the original spring constant values, denoted K_{org}, are considered (see Table IV). The eigenvalues for Case A are shown in Table V. For the set of parameters K_{max}, the SUB mode shifts from 30 to 32 Hz and SSR still arises in the system. Although SUB remains unaffected for set K_{min}, it can be noticed that TM4 is no longer in the neighborhood of SUB and, as a result, the system is no longer unstable for 40% series compensation.

The performance of the proposed SSFDC scheme under torsional stiffness variations is assessed via time-domain simulations. As evidenced by Fig. 17(a), the SSFE scheme is able to identify the new network mode (18 Hz) for parameters K_{max}, which is the complement of SUB (32 Hz). This demonstrates the capability of the SSFE scheme in identifying oscillation frequencies under parametric changes. The damping performance for Case A is shown in Fig. 17(b). As it can be seen, the damper is robust enough to cope with the parametric uncertainty while providing a satisfactory performance.
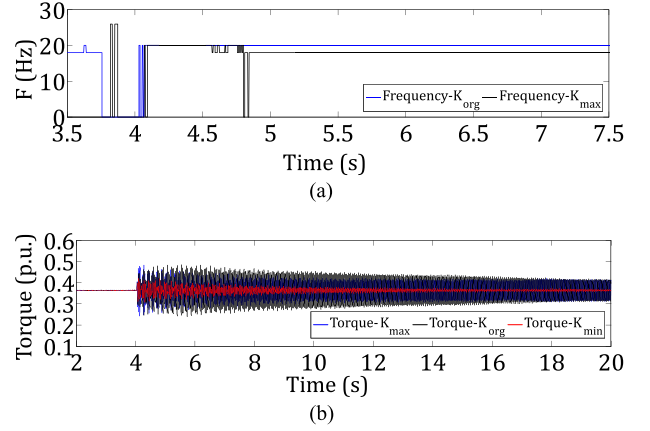

Fig. 17.　Simulation plot for spring constant uncertainty. (a) SSF component estimation. (b) Torque response at 40% series compensation level.
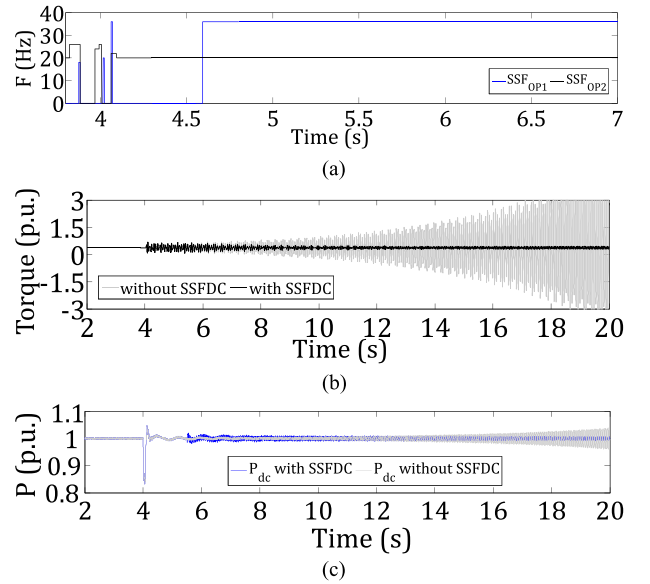

Fig. 18.　Test results for different operating conditions. (a) SSF estimation for OP1 and OP2. (b) Torque response at 110% series compensation level. (c) DC link output power at VSC1 with and without SSFDC for OP2.

B. SSFDC Performance for Extreme Operating Conditions

Two cases are examined to assess the robustness and performance of the SSFDC under extreme operating conditions. In the first one, a very high compensation value is adopted (OP1), while in the second one a large disturbance is considered (OP2).

In OP1, 110% series compensation is employed. This excites TM1 (14 Hz) of the NS generator (see Fig. 3). Fig. 18(a) shows the SSF component in the line current following a change in series compensation from 30 to 110% at $t = 4$ s. It can be seen that the SSFE is able to identify the right SSF component (36 Hz), which is the complement of TM1 (14 Hz). Moreover, the SSFDC is able damp the SSF component, which does not occur in the system without a damper (see Fig. 18(b)).

In OP2, a three-phase-to-ground fault takes place in the series-compensated line. It occurs at $t = 4$ s and has a duration of 75 ms. A 40% compensation level is considered. As it can be
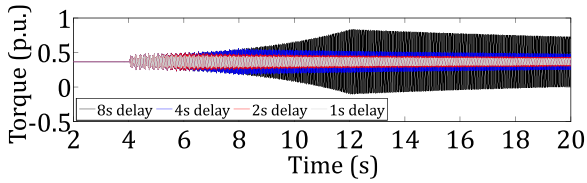
Fig. 19. Torque response showing the influence of time delay in the SSFDC operation.

Fig. 20. Closed-loop system formulated by the linearized mechanical and electrical dynamics.

observed in Fig. 18(a), the SSF component in the line current (20 Hz) is identified after the fault. Without an SSFDC in place, SSR appears following fault clearance, as evidenced by the fluctuations in the dc link power in Fig. 18(c). Conversely, SSR is damped once SSFDC operation is enabled in VSC1.

The results presented in this section confirm the capability of the proposed SSFDC to achieve a robust damping performance upon extreme operating conditions. It should be emphasized though that the quantification of robustness margins when multiple uncertainties and/or operating conditions are considered is out of the scope of this work.

C. Impact of Delays on SSFDC Operation

In the proposed SSFDC scheme, the information to be communicated between the damper and the VSC includes the oscillation frequency and locally measured currents. The amount of data to be transferred is small, which implies limited communication time delays. In addition, it should be borne in mind that SSR may take seconds or even minutes to build-up in a practical power system upon disturbances; thus, communication delays in the range of milliseconds will not affect the SSFDC performance [35], [36]. Although there may be delays present in the control loops of the VSCs, the bandwidth of these loops is much higher than the SSFs; thus, the SSR modes will not be affected [10], [36].

To corroborate the previous assessment, the impact of time delays between the occurrence of SSR and its detection on the performance of the proposed SSFDC is studied. A delay policy of 1 s for the SSFE is adopted, which is considered reasonable compared to other known methods for SSR detection requiring more than 2 s for SSF estimation [37]. This time is considered as sufficient to accommodate for multiple SSF modes due to measurement and parametric uncertainty.

Fig. 19 shows the simulation results for Case A when different time delays on SSF detection are considered. As it can be observed, a delay of 1 s does not have a severe impact on the damping performance. However, the longer it takes to detect the SSF component, the longer it also takes for the torque responses to decrease their magnitudes. It should be highlighted that the damping capability is still preserved even with an arguably large delay time (8 s) in SSF detection—at the expense of increasing torque oscillations for a few seconds.

D. Discussion on System Stability

In this work, stability has been analyzed so far using eigen-analysis. Table I shows the open loop eigenvalues for Cases A
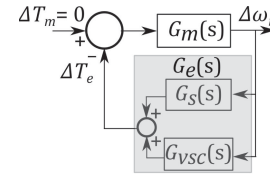
and B without a damping controller, while Table II shows the eigenvalues for the same cases once the SSFDC-upgraded VSC is considered (i.e. once a closed-loop control system is in place). Comparing these results, the previously unstable systems with 40 and 75% compensation levels become stable when a closed-loop control system is included.

Different approaches for stability analysis in SSR studies can be found in the literature. A classical approach is the complex torque coefficient method [10], where the mechanical and electrical systems of a turbo-generator are analyzed separately. However, they are linked through the rotor's speed deviation ($\Delta\omega_r$) and the electromagnetic torque deviation (ΔT_e) that the rotor experiences under a small-signal perturbation. Since the turbine dynamics are inherently slow, the mechanical torque (ΔT_m) is considered as constant. This can be seen in the block diagram shown in Fig. 20, where the electrical network forms a feedback path from $\Delta\omega_r$ to ΔT_e, resulting in a closed-loop system. This includes the transfer functions of the electrical system $G_e(s)$ (which comprises the series-compensated ac system, $G_s(s)$, and the VSC-HVDC link, $G_{VSC}(s)$) and of the mechanical system $G_m(s)$. The open-loop transfer functions $G_e(s)$ and $G_m(s)$ can be considered as stable to represent a practical case [10], [38]. System stability for the open and closed-loop systems can be determined using eigenvalue or electric damping analysis [10], [21].

An alternative approach is to use the positive net damping criterion [38]. In the frequency domain, the electrical and mechanical system dynamics can be expressed as

$$G_e(j\omega) = D_e(\omega) + jK_e(\omega)$$

$$\frac{1}{G_e(j\omega)} = D_m(\omega) + jK_m(\omega) \tag{4}$$

where $D_e(\omega)$ and $D_m(\omega)$ are referred to as the electrical damping and the mechanical damping, respectively. The criterion states that if $D_e(\omega) + D_m(\omega) > 0$, then the closed-loop system in Fig. 20 is asymptotically stable. This implies a low risk of SSR [38]. For realistic systems, $D_m(\omega) > 0$. However, when series-compensated transmission lines and power electronic converters are considered, $D_e(\omega)$ may become negative for low frequencies. For these conditions, the criterion indicates a potential risk of SSR [10], [38].

The electric damping profile of the test system shown in Fig. 1 has been obtained to identify the risk of SSR using the positive net damping criterion, with results shown in Fig. 21. As it can be observed, the damping profile for Cases A (40%) and B (75%) are considerably improved when the SSFDC is in service. This
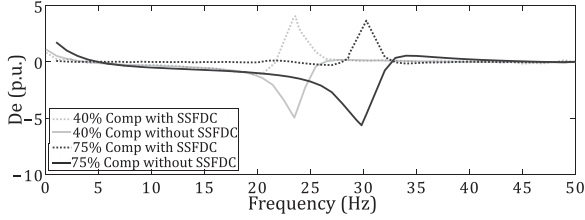
Fig. 21. Electrical damping torque profile for the test system with and without SSFDC.

is achieved as a positive electrical damping is introduced to the system. When the SSFDC is not in operation, the electrical damping is negative around the TM frequencies.

VII. Conclusion

This paper has proposed an adaptive SSR detection and damping scheme. Due to its damping capabilities irrespective of the modes of oscillation being excited, its use is suitable to increase system resiliency against SSR events. An integral part of the proposed scheme is the real-time identification of the SSF component in the presence of multiple torsional modes. As a result, the real-time SSF identification scheme could be applied to any power system in spite of uncertainties in turbo-generator mechanical data.

The SSR phenomenon has been characterized using a reduced GB transmission network incorporating infrastructure reinforcements in the form of series compensation and HVDC links. The risk of SSR occurrence when series compensation is deployed clearly highlights the need for effective countermeasures so as to maintain the security of the network.

The contribution of an HVDC link towards SSR damping has been assessed via eigenanalysis following system state-space modeling. Results illustrate the regions of stability for different compensation levels, with stability being attained regardless of the amount of series compensation once the damper is employed. The proposed SSFDC adapts to different network conditions by acting on the unstable regions of operation resulting from the excitation of different mechanical modes at different compensation levels. An important aspect of the proposed scheme is that the HVDC link is capable of damping SSR upon occurrence while utilizing its existing capacity.

The damping scheme has been tested and validated using time-domain simulations and an RT-HiL experimental platform. Results show that damping provision does not interfere with the power transfer capability or the stability of the HVDC link. The provision of active power transfer and SSR damping using the same link rather than incorporating additional damping devices represents an enhanced asset utilization.

Even when the proposed solution works well, practical limitations requiring further investigation have been identified. The time to detect SSR and the precision of the frequency estimation rely on the signal processing method employed. In this work, FFT was adopted; however, other less computationally intensive and more efficient signal processing techniques may be employed instead. It should be also highlighted that local measurements are used as input signals to the dampers

and current injection is performed by the VSC closest to the generator exhibiting torsional oscillations. If a VSC station is not sufficiently close, the damping controllers proposed in this work could be implemented in a nearby power electronic-based controller (e.g., an SVC, a TCSC or a STATCOM).

Appendix

A. Mathematical Derivation for SSF Component Estimation

A generator connected to a compensated line is considered to derive an expression of the voltage's subsynchronous component at the generator terminals. The interaction between electrical and mechanical systems is simulated by applying an oscillating speed to the generator shaft. The voltage (p.u.) at the generator terminals can be written in the $\alpha\beta$-frame as [3], [37]

$$\bar{e}^{\alpha\beta}(t) = e^{\alpha}(t) + je^{\beta}(t)$$
$$= \bar{\omega}(t)E_g\cos(\omega_0 + \delta(t)) + j\sin(\omega_0 t + \delta(t)) \quad (5)$$

where E_g is the amplitude of the terminal voltage at rated speed, δ its phase displacement, $\bar{\omega}$ the rotor speed (p.u.), and ω_0 the fundamental frequency (rad/s). If the rotor oscillates around ω_0, its speed (p.u.) is given by

$$\bar{\omega}(t) = \bar{\omega}_0 + A\sin(\omega_m t) \quad (6)$$

where A is the amplitude of the oscillation and ω_m is the oscillation frequency (rad/s) of the rotor. Substituting (6) in (5), the α-axis component of the output voltage is written as

$$e^{\alpha}(t) = [\bar{\omega}_0 + A\sin(\omega_m t)]E_g\cos(\omega_0 t + \delta(t))$$
$$= \bar{\omega}_0 E_g\cos[\omega_0 t + \delta(t)] + \frac{AE_g}{2}[-\sin(\omega_0 - \omega_m)t + \delta(t)$$
$$+ \sin(\omega_0 + \omega_m)t + \delta(t)] \quad (7)$$

The derivative of the rotor angle δ is given as

$$\frac{d\delta(t)}{dt} = [\bar{\omega}(t) - \bar{\omega}_0]\omega_B = A\sin(\omega_m t)\omega_B \quad (8)$$

where ω_B is the base frequency (rad/s). Substituting (6) in (8) yields

$$\delta(t) = \delta_0 - A\frac{\omega_B}{\omega_m}\cos(\omega_m t) \quad (9)$$

where δ_0 is the rotor angle in steady-state. Following the substitution of (7) in (9) and after performing algebraic reductions,

$$e^{\alpha}(t) = \bar{\omega}_0 E_g\cos(\omega_0 t + \delta_0) + \frac{AE_g}{2\omega_m}[(\omega_0 - \omega_m)$$
$$\sin(\omega_0 - \omega_m)t + \delta_0] + (\omega_0 - \omega_m)\sin(\omega_0 + \omega_m)t + \delta_0]. \quad (10)$$

Similarly, the β-axis component of the voltage is obtained as

$$e^{\beta}(t) = \bar{\omega}_0 E_g\sin(\omega_0 t + \delta_0) + \frac{AE_g}{2\omega_m}[-(\omega_0 - \omega_m)$$
$$\cos(\omega_0 - \omega_m)t + \delta_0] - (\omega_0 + \omega_m)\cos(\omega_0 + \omega_m)t + \delta_0]. \quad (11)$$

Assuming the amplitude of A is small, it can be seen from (10) and (11) that the induced voltage in the stator has three terms:

one at rated frequency and two at frequencies $\omega_0 \pm \omega_m$. The subsynchronous components are

$$e_{sub}^{\alpha}(t) = \frac{AE_g}{2\omega_m}[(\omega_0 - \omega_m)\sin(\omega_0 - \omega_m)t + \delta_0]$$

$$e_{sub}^{\beta}(t) = -\frac{AE_g}{2\omega_m}[(\omega_0 - \omega_m)\cos(\omega_0 - \omega_m)t + \delta_0] \quad (12)$$

Voltages in (12) cause SSF current to flow. Current components are given by

$$(i_{sub}^{\alpha}(t) + ji_{sub}^{\beta}(t)) = Z^{-1}[j(\omega_0 - \omega_m)](e_{sub}^{\alpha}(t) + je_{sub}^{\beta}(t)) \quad (13)$$

Considering $Z(s) = R + Ls + 1/Cs$,

$$Z[j(\omega_0 - \omega_m)] = R + \left[j(\omega_0 - \omega_m)L - \frac{1}{(\omega_0 - \omega_m)C}\right]$$

$$= Z_{sub}\angle\phi_{sub} \quad (14)$$

where R, L, C are the resistance, inductance and capacitance of the network and $Z_{sub}\angle\phi_{sub}$ the network impedance at SSF as viewed from the generator internal bus. The dq-axis subsynchronous current components of (13) are

$$i_{sub}^{dq}(t) = e^{-j(\omega_0 t + \delta)}i_{sub}^{\alpha\beta}(t)$$

$$= -\frac{AE_g}{2\omega_m Z_{sub}}(\omega_0 - \omega_m)e^{-j(\omega_m t + \phi_{sub})} \quad (15)$$

Finally, the torque component due to the subsynchronous current is given by

$$T_{sub}^e = E_g i_{sub}^d$$

$$= -\frac{A(E_g)^2}{2\omega_m Z_{sub}}(\omega_0 - \omega_m)\sin(\omega_m t + \phi_{sub}) \quad (16)$$

From (15), the SSF component can be estimated by applying suitable signal processing approaches [20]. To this end, (3) is written as

$$\underbrace{i^{dq}(t)}_{s(t)} = \underbrace{i_f^{dq}(t)}_{x(t)} + \underbrace{i_{sub}^{dq}(t) + i_{sup}^{dq}(t)}_{g(t)} \quad (17)$$

With reference to Fig. 4 and (17), the subsynchronous component is isolated from the line current by removing the fundamental and supersynchronous components. This is achieved with a low-pass filter and a comparator block. The remaining component is $i_{sub}^{dq}(t)$, shown in (15). It is assumed that this is a continuous periodic real-valued signal $g(t)$, which can be expanded using a Fourier series. The general form of the Fourier series can be written as

$$F(t) = \sum_0^k g(t)e^{j\omega_{km}t}, \; g(t) = \frac{1}{T}\int_0^k g(t)e^{-j\omega_{km}t} \quad (18)$$

The Fourier transform of (18), sampled at F_s for a window length of T from k_0 to $(k_0 + T)$, can be written as

$$F(\omega) = \sum_{n=k_0}^{k_0+T} g(n)e^{-j\omega_{km}} \quad (19)$$

The frequency spectrum will have m peaks—one for each torsional oscillation frequency component [14]. The Fourier transform for each mode becomes

$$F(\omega) = \sum_{n=k_0}^{k_0+T} A_m e^{-\sigma_m k}\cos(\omega_m k + \phi_{sub})e^{-j\omega_{km}} \quad (20)$$

$F(\omega)$ in (20) is used to calculate the oscillatory frequency f_i in Fig. 4, where

$$f_i = \frac{\text{argmax}_\omega |F(\omega)|}{2\pi} \quad (21)$$

Equations (17)–(21) provide the mathematical implementation of the SSFE process described in Section II.

B. Control System Parameters of the VSC-HVDC Link

The PI controllers are represented in the form: $K(s) = K_p + K_i/s$. Two-level VSCs: Current: $K_p = 50$, $K_i = 15000$. DC voltage: $K_p = 0.2$, $K_i = 200$. Active power: $K_p = 0.2$, $K_i = 200$. Reactive power: $K_p = 0.2$, $K_i = 200$.

REFERENCES

[1] Subsynchronous Resonance Working Group, "Reader's guide to subsynchronous resonance," *IEEE Trans. Power Syst.*, vol. 7, no. 1, pp. 150–157, Feb. 1992.

[2] P. M. Anderson, B. L. Agrawal, and J. E. Van Ness, *Subsynchronous Resonance in Power Systems*. Piscataway, NJ, USA: IEEE Press, 1990.

[3] K. R. Padiyar, *Analysis of Subsynchronous Resonance in Power Systems*. Boston, MA, USA: Kluwer, 1999.

[4] National Grid, *Electricity Ten Year Statement 2014*. Warwick, U.K.: National Grid UK, 2014.

[5] National Grid, *System Operability Framework 2015*. Warwick, U.K.: National Grid UK, 2015.

[6] N. Flourentzou, V. G. Agelidis, and G. D. Demetriades, "VSC-Based HVDC power transmission systems: An overview," *IEEE Trans. Power Electron.*, vol. 24, no. 3, pp. 592–602, Mar. 2009.

[7] M. Bahrman and E. V. Larsen, "Experience with HVDC—Turbine-generator torsional interaction at square butte," *IEEE Trans. Power App. Syst.*, vol. PAS-99, no. 3, pp. 966–975, May 1980.

[8] N. Prabhu and K. R. Padiyar, "Investigation of subsynchronous resonance with VSC-based HVDC transmission systems," *IEEE Trans. Power Del.*, vol. 24, no. 1, pp. 433–440, Jan. 2009.

[9] D. Sun, X. Xie, Y. Liu, K. Wang, and M. Ye, "Investigation of SSTI between practical MMC-based VSC-HVDC and adjacent turbogenerators through modal signal injection test," *IEEE Trans. Power Del.*, vol. 32, no. 6, pp. 2432–2441, Dec. 2017.

[10] L. Harnefors, "Analysis of subsynchronous torsional interaction with power electronic converters," *IEEE Trans. Power Syst.*, vol. 22, no. 1, pp. 305–313, Feb. 2007.

[11] L. Wang, X. Xie, Q. Jiang, H. Liu, Y. Li, and H. Liu, "Investigation of SSR in practical DFIG-based wind farms connected to a series-compensated power system," *IEEE Trans. Power Syst.*, vol. 30, no. 5, pp. 2772–2779, Sep. 2015.

[12] X. Xie, C. Zhang, H. Liu, C. Liu, D. Jiang, and B. Zhou, "Continuous-mass-model-based mechanical and electrical co-simulation of SSR and its application to a practical shaft failure event," *IEEE Trans. Power Syst.*, vol. 31, no. 6, pp. 5172–5180, Nov. 2016.

[13] T. Rauhala, A. M. Gole, and P. Järventausta, "Detection of subsynchronous torsional oscillation frequencies using phasor measurement," *IEEE Trans. Power Del.*, vol. 31, no. 1, pp. 11–19, Feb. 2016.

[14] Z. Tashman, H. Khalilinia, and V. Venkatasubramanian, "Multi-dimensional fourier ringdown analysis for power systems using synchrophasors," *IEEE Trans. Power Syst.*, vol. 29, no. 2, pp. 731–741, Mar. 2014.

[15] M. Ayar, S. Obuz, R. D. Trevizan, A. S. Bretas, and H. A. Latchman, "A distributed control approach for enhancing smart grid transient stability and resilience," *IEEE Trans. Smart Grid*, vol. 8, no. 6, pp. 3035–3044, Nov. 2017.

[16] M. Ayar, R. D. Trevizan, S. Obuz, A. S. Bretas, H. A. Latchman, and N. G. Bretas, "Cyber-physical robust control framework for enhancing transient stability of smart grids," *IET Cyber-Phys. Syst.: Theory Appl.*, vol. 2, no. 4, pp. 198–206, Dec. 2017.

[17] T. Rajaram, J. M. Reddy, and Y. Xu, "Kalman filter based detection and mitigation of subsynchronous resonance with SSSC," *IEEE Trans. Power Syst.*, vol. 32, no. 2, pp. 1400–1409, Mar. 2017.

[18] K. R. Padiyar and N. Prabhu, "Design and performance evaluation of subsynchronous damping controller with STATCOM," *IEEE Trans. Power Del.*, vol. 21, no. 3, pp. 1398–1405, Jul. 2006.

[19] M. Bongiorno, J. Svensson, and L. Angquist, "Single-phase VSC based SSSC for subsynchronous resonance damping," *IEEE Trans. Power Del.*, vol. 23, no. 3, pp. 1544–1552, Jul. 2008.

[20] M. Bongiorno, L. Angquist, and J. Svensson, "A novel control strategy for subsynchronous resonance mitigation using SSSC," *IEEE Trans. Power Del.*, vol. 23, no. 2, pp. 1033–1041, Apr. 2008.

[21] M. Bongiorno, J. Svensson, and L. Angquist, "On control of static synchronous series compensator for SSR mitigation," *IEEE Trans. Power Electron.*, vol. 23, no. 2, pp. 735–743, Mar. 2008.

[22] L. Wang, X. Xie, Q. Jiang, and H. R. Pota, "Mitigation of multimodal subsynchronous resonance via controlled injection of supersynchronous and subsynchronous currents," *IEEE Trans. Power Syst.*, vol. 29, no. 3, pp. 1335–1344, May 2014.

[23] R. Thirumalaivasan, M. Janaki, and N. Prabhu, "Damping of SSR using subsynchronous current suppressor with SSSC," *IEEE Trans. Power Syst.*, vol. 28, no. 1, pp. 64–74, Feb. 2013.

[24] X. Xie, L. Wang, X. Guo, Q. Jiang, Q. Liu, and Y. Zhao, "Development and field experiments of a generator terminal subsynchronous damper," *IEEE Trans. Power Electron.*, vol. 29, no. 4, pp. 1693–1701, Apr. 2014.

[25] J. Zhang *et al.*, "Suppressing intermittent subsynchronous oscillation via subsynchronous modulation of reactive current," *IEEE Trans. Power Del.*, vol. 30, no. 5, pp. 2321–2330, Oct. 2015.

[26] K. M. Alawasa and Y. A.-R. I. Mohamed, "A simple approach to damp SSR in series-compensated systems via reshaping the output admittance of a nearby VSC-based system," *IEEE Trans. Ind. Electron.*, vol. 62, no. 5, pp. 2673–2682, May 2015.

[27] IEEE Subsynchronous Resonance Task Force of the Dynamic System Performance Working Group Power System Engineering Committee, "First benchmark model for computer simulation of subsynchronous resonance," *IEEE Trans. Power App. Syst.*, vol. 96, no. 5, pp. 1565–1572, Sep. 1977.

[28] IEEE Subsynchronous Resonance Working Group of the Dynamic System Performance Subcommittee Power System Engineering Committee, "Second benchmark model for computer simulation of subsynchronous resonance," *IEEE Trans. Power App. Syst.*, vol. 104, no. 5, pp. 1057–1066, May 1985.

[29] L. Livermore, C. E. Ugalde-Loo, Q. Mu, J. Liang, J. B. Ekanayake, and N. Jenkins, "Damping of subsynchronous resonance using a voltage source converter-based high-voltage direct-current link in a series compensated Great Britain transmission network," *IET Gener. Trans. Distrib.*, vol. 8, no. 3, pp. 542–551, Mar. 2014.

[30] C. E. Ugalde-Loo, J. B. Ekanayake, and N. Jenkins, "Subsynchronous resonance in a series-compensated Great Britain transmission network," *IET Gener. Trans. Distrib.*, vol. 7, no. 3, pp. 209–17, Mar. 2013.

[31] C. E. Ugalde-Loo, J. B. Ekanayake, and N. Jenkins, "Subsynchronous resonance on series compensated transmission lines with quadrature boosters," in *Proc. IEEE Trondheim PowerTech*, Trondheim, Norway, 2011, pp. 802–808.

[32] T. Joseph, C. E. Ugalde-Loo, and J. Liang, "Subsynchronous oscillatory stability analysis of an ac/dc transmission system," in *Proc. IEEE Eindhoven PowerTech*, Eindhoven, Netherlands, 2015, pp. 1–6.

[33] T. Joseph, C. E. Ugalde-Loo, J. Liang, and P. Coventry, "Active filtering based current injection method for multi modal SSR damping in an ac/dc system," in *Proc. 17th Euro. Conf. Power Electron. Appl.*, Geneva, Switzerland, 2015, pp. 1–10.

[34] J. V. Milanovic, "The influence of shaft spring constant uncertainty on torsional modes of turbogenerator," *IEEE Trans. Energy Convers.*, vol. 13, no. 2, pp. 170–175, Jun. 1998.

[35] X. Xie, W. Liu, H. Liu, Y. Du, and Y. Li, "A system-wide protection against unstable SSCI in series-compensated wind power systems," *IEEE Trans. Power Del.*, to be published, doi: 10.1109/TPWRD.2018.2829846.

[36] L. Zeni *et al.*, "Power oscillation damping from VSC–HVDC connected offshore wind power plants," *IEEE Trans. Power Del.*, vol. 31, no. 2, pp. 829–838, Apr. 2016.

[37] M. Bongiorno, J. Svensson, and L. Angquist, "Online estimation of subsynchronous voltage components in power systems," *IEEE Trans. Power Del.*, vol. 23, no. 1, pp. 410–418, Jan. 2008.

[38] L. Harnefors, "Proof and application of the positive-net-damping stability criterion," *IEEE Trans. Power Syst.*, vol. 26, no. 1, pp. 481–482, Feb. 2011.

Tibin Joseph (S'13–M'16) received the B.Tech. and M.Tech degrees in electrical engineering from Mahatma Gandhi University, Kottayam, India, in 2008 and 2011, respectively, and the Ph.D degree in electrical and electronic engineering from Cardiff University, Cardiff, U.K., in 2018. From 2012 to 2013, he worked as a Lecturer with Saintgits College of Engineering, Kottayam, India. He was a Marie Curie Early Stage Researcher between 2013 and 2016 with Cardiff University. He has been a Visiting Researcher with CEPRI, Beijing, China, and with National Grid UK, Warwick, U.K. Since 2016, he has been working as a Research Associate with Cardiff University.

Carlos E. Ugalde-Loo (M'02) was born in Mexico City. He received the B.Sc. degree in electronics and communications engineering from Instituto Tecnológico y de Estudios Superiores de Monterrey, Mexico City, in 2002, the M.Sc. degree in electrical engineering from Instituto Politcnico Nacional, Mexico City, México, in 2005, and the Ph.D. degree in electronics and electrical Engineering from the University of Glasgow, Scotland, U.K., in 2009.

In 2010, he joined the School of Engineering, Cardiff University, Cardiff, U.K., and is currently a Reader in Electrical Power Systems. His research interests include power system stability and control, grid integration and control of renewables, HVDC transmission, integrated energy systems, modeling of dynamic systems, and multivariable control.

Senthooran Balasubramaniam (S'12) received the B.Eng. (Hons.) degree in electronic engineering from the University of Surrey, Guildford, U.K., in 2012, and the Ph.D. degree in electrical and electronic engineering from Cardiff University, Cardiff, U.K., in 2017.

He is currently a Postdoctoral Researcher with the Energy Safety Research Institute, Swansea University, Swansea, U.K. His research interests include HVDC technologies, power electronics, grid integration of renewable energy, and power system control and stability.

Jun Liang (M'02–SM'12) received the B.Sc. degree from Huazhong University of Science and Technology, Wuhan, China, in 1992, and the M.Sc. and Ph.D. degrees from China Electric Power Research Institute, Beijing, China, in 1995 and 1998, respectively. From 1998 to 2001, he was a Senior Engineer with China Electric Power Research Institute. From 2001 to 2005, he was a Research Associate with Imperial College London, London, U.K. From 2005 to 2007, he was a Senior Lecturer with the University of Glamorgan, Wales, U.K.

He is currently a Professor with the School of Engineering, Cardiff University, Cardiff, U.K. His research interests include FACTS devices/HVDC, power system stability and control, power electronics, and renewable power generation.